Electrochimica Acta 440 (2023) 141732

Contents lists available at ScienceDirect

Electrochimica Acta

journal homepage: www.journals.elsevier.com/electrochimica-acta

Electrochemical properties of graphite/nylon electrodes additively manufactured by laser powder bed fusion

Olga Pastushok [a,*], Lauri Kivijärvi [c], Ekaterina Laakso [b], Matti Haukka [c], Heidi Piili [d], Eveliina Repo [b]

[a] Department of Separation Science, School of Engineering Science, Lappeenranta-Lahti University of Technology (LUT), Sammonkatu 12, Mikkeli, FI-50130, Finland
[b] Department of Separation Science, School of Engineering Science, Lappeenranta-Lahti University of Technology (LUT), Yliopistonkatu 34, Lappeenranta, FI-53850, Finland
[c] Department of Chemistry, University of Juväskylä, Survontie 9 B, Jyväskylä, FI-40024, Finland
[d] Department of Mechanical and Materials Engineering, University of Turku, Joukahaisenkatu 3-5, Turku, FI-20520, Finland

ARTICLE INFO

Keywords:
Graphite
Nylon
Electrodes
Additive manufacturing
Laser powder bed fusion

ABSTRACT

Nowadays, additive manufacturing, known as 3D printing, is vigorously employed at various enterprises due to the ability of industrial series production and customization in conjunction with geometry freedom. While, material design and fabrication of composite materials, meeting the desired architecture and properties, is another promising application of additive manufacturing. For instance, additive manufacturing of the material exhibiting electrochemical properties is beneficial for the development of freestanding electrodes that might be used in electrochemical energy storage systems. Herein, the graphite/nylon composite with a high carbon ratio of 30 wt% was produced by laser powder bed fusion to promote the development of the additive manufacturing of electrochemical energy storage devices. The material characterization of the additively manufactured graphite/nylon electrode demonstrates the porous structure with uniform distribution of the compounds, and the absence of chemical interactions between them during laser powder bed fusion. The electrochemical properties of the composite were investigated in acidic, neutral, and alkaline electrolytes. The tested additively manufactured electrodes demonstrate a capacitive behaviour and a stable electrochemical performance with average capacitance retention of 95%. The findings open new frontiers for the development and improvement of the production of electrochemically active materials by additive manufacturing with consideration to design freedom and customization.

1. Introduction

Sustainable and clean energy sources are a worldwide priority nowadays [1]. Electrochemical energy storage (EES) systems are designated for aiding the development of energy technologies via harvesting and distribution of the excess produced energy [2]. Among different EES systems, supercapacitors (SCs), based on the electrostatic double layer (EDL), are of the utmost interest due to the rapid charging and discharging, accompanied by excellent cyclability [3,4]. Typically, supercapacitors consist of a pair of porous carbon electrodes, separated by an insulating material saturated with an electrolyte. Capacitive electrodes are a significant part of SCs. The current method of capacitive electrode production, carbon slurry casting, is limited by the customized architecture [5] and challenges associated with the fluidic properties (viscosity, surface tension, and aggregation of carbon particles) and toxicity of a slurry [6]. Additionally, an appropriate substrate (current collector) is typically required for such electrodes. Thus, there is a growing demand for new materials applied in EES [7].

Emerging additive manufacturing (AM) techniques, commonly called 3D printing, can be incorporated into the production of EES systems. Therefore, components for electrochemical cells or even full systems can be produced via a single-step manufacturing process resulting in customizable objects with complex geometries and lower weight [8]. The geometry freedom, provided by AM, is particularly topical for brittleness carbon materials, ensuring controllable size, shape, flow properties, and bringing well-known materials into a new perspective. The advanced design and complex geometric shapes, implemented in the EES systems, have recently been demonstrated via a rolled capacitor

* Corresponding author.
E-mail address: olga.pastushok@lut.fi (O. Pastushok).

https://doi.org/10.1016/j.electacta.2022.141732
Received 27 June 2022; Received in revised form 9 December 2022; Accepted 16 December 2022
Available online 20 December 2022

based on the conductive acrylonitrile butadiene styrene (ABS) [9], a flexible multilayer composite capacitor [10], and a parallel plates capacitor with black polylactic acid (PLA) separator [11], additively manufactured in a single print. Nevertheless, specific attention should be paid to the material properties of the AM objects to meet the requirements of the capacitive electrodes: electrical conductivity, high surface area, and electrochemical activity. Despite, about 3800 AM materials being commercially available nowadays [12], most of them are presented by non-conductive polymers and ceramics, which are improper as capacitive electrodes. Therefore, composites consisting of a polymer matrix material, supporting the AM process, and reinforcement material, introducing required properties, are used to comply with the capacitive electrodes.

AM carbon-based composites have grasped enormous research interest recently due to the enhancement of mechanical properties and the introduction of electrical conductivity to matrix materials [13]. However, the existing AM carbon-based composites suffer from insufficient electrical conductivity, poor porosity, and low hydrophilicity, caused by a high ratio of a polymeric material and resulting in dramatic limitations for their utilization as electrodes in EES systems. The number of the existing carbon-based composites, which were electrochemically tested, is not very high nowadays. The electrochemical properties of state-of-the-art AM carbon-based electrodes are summarized in Table S1 (Supplemental materials). It might be noticed that the typical AM process for the fabrication of carbon-based composites is material extrusion (ME), which includes fused deposition modeling (FDM) and direct ink writing (DIW). The commonly used polymer and the conductive carbon additive are assigned to polylactic acid (PLA) and graphene, respectively. It is inappropriate to consider an average value of the specific capacitance that the available AM materials could reach because there is no universal protocol for the electrochemical investigation. Nevertheless, the highest possible value of the specific capacitance of 4.79 F cm^{-2} was achieved by graphene oxide/graphene nanoplatelet/fumed silica composite additively manufactured by DIW and electrochemically tested in 3 M KOH electrolyte at 0.4 A g^{-1} applied current density [14]. The lowest reported value of the specific capacitance of 17.17 μF cm^{-2} was obtained using 8 wt% graphene/PLA composite, produced by FDM and tested in H_2SO_4 electrolyte under 0.5 μA.

As it was mentioned above, most studies refer to material extrusion-based AM process, because of its easy operation, low cost, and a wide choice of materials [15]. Despite the variety of conductive inks and filaments, the production of porous electrodes by the ME processes is unrealizable without a special design of flow channels providing a vast surface area available for an electrolyte. The dense structure of the ME-printed objects is caused by the manufacturing method itself, where the input materials are completely melted or present in a viscous form, and then go through solidification [16]. While originally porous AM electrodes can be printed by laser powder bed fusion (L-PBF). This is possible due to its operating principle, in which "thermal energy is selectively deposited to join powder materials" [17]. Therefore, neither pressure nor shear flow affects the dispersion of solid particles in the L-PBF printing, and a porous structure is created. The composition of AM materials for the L-PBF process can be prepared with minimal pre-processing requirements such as mixing of powder input materials. Therefore, the polymer/conducting additive material ratio can be easily adjusted with the only limitation of the sufficient durability of the printed objects. The maximum graphite loading of 40 wt% can be used for printing by L-PBF [18]. Whereas, the ME process requires specially prepared filaments or inks, in which the concentration of conductive additives is limited by 10 wt% because of the inhomogeneous dispersion resulting in the agglomeration of solid particles [19]. Additionally, L-PBF allows the printing of complex objects without using supporting structures, resulting in the reduction of the loss of the printing material. While support structures are required for ME processes to prevent the overhang deformation of printed objects.

Carbon-based composites, printed by L-PBF, have been already reported and examined for mechanical and thermal properties [20–23]. Additionally, these composites demonstrate electrical conductivity, which directly depends on the ratio of carbon material [18] and the percolation threshold [24]. The recent developments in L-PBF-manufactured carbon-based composites are presented in Table S2. The number of the reported L-PBF-produced carbon-based composites is less than the ME-produced conductive objects (in Table S1). Typically, nylon (polyamide 12) is used as a polymer, and carbon black as a conductive additive in the printing mixtures in the L-PBF process. Being porous and electrically conductive (the listed in Table S2 composites represent an electrical conductivity from 14×10^{-5} S cm^{-1} to $\sim 1 \times 10^{-2}$ S cm^{-1}), these L-PBF-manufactured carbon-based composites might exhibit an electrochemical activity that has not been investigated yet, to the best of our knowledge. Therefore, this study is motivated by the possibility of L-PBF to print originally porous and conductive electrodes aimed to bridge the gap in the electrochemical study on this type of electrodes.

Herein, the research on the AM graphite/nylon electrodes is continued within the application of various electrochemical techniques to launch the initiative and estimate the prospects of this composite material to be used as freestanding electrodes in EES systems. The choice of additive manufacturing compounds was caused by the conventionality and availability of the materials allowing technology adjustment. Nylon dominates among other semi-crystalline polymers utilized in L-PBF because of its proper mechanical and thermal properties [25], providing a durable AM matrix. Whereas graphite with the electrical conductivity of (ca. 63×10^{-2} S cm^{-1}) [18] is one of the commonly used carbon materials, widely applied in the production of EES systems.

2. Experimental section

2.1. Additive manufacturing of the graphite/nylon electrodes

A mixture of commercial nylon (polyamide 12) with an average particle diameter of 50 μm, gained from ADVANC3D Materials (Germany), and synthetic graphite powder (<20 μm), purchased from Sigma Aldrich (USA), were used as a printing material for electrodes. The supporting polymer and graphite were mixed carefully by mechanical agitation of the components and shaking them in a closed vessel until uniform material was obtained. The graphite loading of 30 wt% in the printing mixture enables a relatively high electric conductivity (ca. 1×10^{-2} S cm^{-1}) and sufficiently high mechanical strength of the AM specimens.

FreeCAD v.0.16 and Slic3r v. 1.2.9 software were, respectively, used to design the electrodes and slice the model into two-dimensional. Sharebot SnowWhite 3D printer (Italy) was used for graphite/nylon electrode manufacturing by L-PBF. The following process parameters were applied: the laser power of 8.4 W, the laser scan speed of 1.28 m s^{-1}, the powder bed temperature of 164 – 167 °C, and the power layer thickness of 0.08 mm.

The AM graphite/nylon electrodes were carefully cleaned from all unsintered powder, rinsed with DI water, and dried in a vacuum oven at 50 °C overnight before use. Digital images of the AM graphite/nylon electrode and its printing dimensions are shown in Fig. S1 and Fig. S2. The average mass and active working area of the AM electrode are 6.85 g and 27 cm^2, respectively.

2.2. Material characterization of the AM graphite/nylon electrode

The morphology, microstructure, and elemental composition of the AM graphite/nylon composite were observed by scanning electron microscopy (SEM) using Jeol JSM-7900F microscope (Japan) equipped with energy-dispersive X-ray spectroscopy (EDX) system, applying an accelerating voltage of 20 kV. Thin sample slices from the electrode surface and cross-section were coated with a thin layer of Pt before SEM analyses. Cross-sections were prepared by cryofracturing a piece of the AM graphite/nylon composite under liquid nitrogen and subsequently

kept in a desiccator before imaging. JEOL JIB-4700F microscope (Japan) was employed for the investigation of the surface morphologies of the bare graphite and nylon powders with SEM accelerating voltage of 15 kV and 1 kV, respectively. Additionally, a cross-section sample of the AM graphite/nylon electrode was prepared with focused ion beam (FIB) milling using Ga^+ ions accelerated at 15 kV and 0.5 nA beam current by a JIB-4700F dual beam system. The analyzed specimen was coated with a 0.6 μm thick carbon layer to avoid Ga-ion beam damage.

A piece of the AM graphite/nylon composite was milled into powder (using IKA tube mill (Germany)) and the input materials were analyzed as received for the below-listed analyses. Brunauer-Emmet-Teller (BET) specific surface area was determined by N_2 adsorption/desorption measurements at 77 K using Micromeritics 3Flex 3500 analyzer (USA), equipped with VacPrep 061 pretreatment unit. The sample materials were pre-treated by degassing under a vacuum at 60°C for 20 h. Crystalline structure was evaluated by X-ray powder diffraction (XRD) using Bruker D8 Advance diffractometer (Germany) with Cu Kα irradiation (λ = 1.5406 Å). Bragg's law was applied to calculate *d*-spacings. Surface functionalities were detected using FTIR-spectrophotometer from Perkin Elmer Frontier (USA) with a universal ATR module (Diamond crystal). Further, the composition, phases, and defects of the compounds (the AM graphite/nylon electrode was analysed as a sliced sample) were observed by Raman spectroscopy using Thermo Scientific DXR3xi imaging microscope (USA), equipped with a green laser (λ =532 nm).

The resistivity of AM graphite/nylon specimen (2 × 10 × 10 mm (thickness/width/length)) was measured by Keithley 6517A electrometer/high resistance meter (USA) at room temperature. As the electrical conductivity is inverse to resistivity (R = 1/C, where R is resistivity and C is electrical conductivity), the value of the electrical conductivity was calculated from this reciprocal proportion.

2.3. Electrochemical characterization

The electrochemical characterization has been performed using a symmetrical two-electrode cell containing a pair of AM graphite/nylon electrodes, separated by a glass microfiber filter (VWR glass microfibres filter grade 696 (USA)), saturated with an electrolyte. Three two-electrode cells were individually tested in acidic, neutral, and alkaline environments using 1 M H_2SO_4 (0.8 S cm^{-1}, pH 0), 1 M NaCl (0.09 S cm^{-1}, pH 6), and 6 M KOH (0.6 S cm^{-1}, pH 14) electrolytes, respectively. The electrolyte solutions were prepared from the chemical reagents of ACS grade, purchased from Sigma Aldrich (USA). The electrodes were analysed by cyclic voltammetry (CV), galvanostatic charge-discharge (GCD), and electrochemical impedance spectroscopy (EIS) using Ivium OctoStat5000 potentiostat (Netherlands). CV curves were recorded at the scan rate from 5 to 100 mV s^{-1}. GCD test has been carried out at the current densities, determined by the corresponding anodic current at 0.4 V from CV curves. EIS was conducted between 1 MHz and 1 mHz applying 1 mA amplitude. The value of the current density used for the data representation has been calculated based on the active working area of two electrodes (54 cm^2).

Capacitance represents the charge, stored between two electrodes, resulting in the formation of an electrostatic field at the applied voltage [4]. The areal specific capacitances are calculated from the data obtained from CV, GCD, and EIS measurements by the equations from Table 1. The measurements were repeated with triplicates, and standard error bars were attached to the values of specific capacitance.

3. Results and discussion

3.1. Material characterization

A composite containing 70 wt% of nylon and 30 wt% of graphite was additively manufactured by L-PBF. To investigate the obtained structure of the AM composite SEM analysis was carried out. Primarily, the SEM images of bare nylon and graphite particles were taken to identify them in the additively manufactured composite. As depicted in Fig. 1(A), graphite particles are presented as thin and plate flakes with sharp edges. While nylon particles demonstrate semi-spherical geometry with an irregular surface, as shown in Fig. 1(B).

A digital image of the AM graphite/nylon electrode is shown in Fig. 2 (A). It can be seen that the AM graphite/nylon electrode has a nonuniform surface. Tiny light spots on the electrode surface correspond to the graphite flakes, which reflect daylight. However, a digital shoot cannot provide a detailed image of the electrode surface. Therefore, a thin slice from the AM electrode surface was investigated by SEM. As shown in Fig. 2(B), the electrode surface is presented as a coarse-grain texture containing many accessible voids. To demonstrate, that a similar porous structure is observed across the whole width of the AM graphite/nylon electrode, a cryofractured cross-section imaging has been performed. The collated SEM images under increasing magnification from the electrode surface and cross-section area are represented in Fig. S3.

Under the higher SEM magnification, it was observed, that the course-grain texture of the composite is formed by spherical shape agglomerates with an approximate diameter of 50 – 70 μm (Fig. 2(C)), related to the partially fused nylon particles [18]. Furthermore, plane particles, attached to the surface of the nylon agglomerates, correspond to graphite flakes. The graphite flakes cover the surface of a nylon agglomerate irregularly. As shown in **Fig. 2**(D), the graphite flakes are overlayed by each other or placed separately at some sites onto the surface of the nylon agglomerate.

To investigate the distribution of the graphite flakes among the AM composite, a cryofractured cross-section area of the nylon agglomerate has been imaged by SEM. Graphite flakes, demonstrating a plane surface with sharp edges, are observed at the cross-section of the nylon agglomerate in **Fig. 2** (E and F). Despite, the nylon particles being joined, not completely melted, a part of the graphite flakes has been encapsulated in the nylon agglomerates during the L-PBF process.

Additionally, a cross-section area of the graphite/nylon agglomerate has been prepared by FIB and further analyzed by EDX to determine the elemental composition inside the fused nylon particles. The analyzed graphite/nylon agglomerate, composed of several fused particles, as depicted in Fig. 3(A). The cross-section area, emphasized with a white frame, was positioned in the joining area of the particles. A stick-like object different in color, compared to the surrounding, was observed by the SEM and shown in Fig. 3(B).

To identify the nature of the object, EDX mapping was performed. Fig. 3(C) represents the distribution of carbon, which trend repeats the stick-like shape of the observed object. While that stick-like area remains blank in the EDX mapping of nitrogen (Fig. 3(D)) and oxygen (Fig. 3(E)).

Table 1
Equations for the calculation of the areal specific capacitance.

Areal specific capacitance (F cm^{-2})	CV	GCD	EIS
C_s	$\frac{\oint i dV}{s \cdot V \cdot A}$	$\frac{I \cdot dt}{dV \cdot A}$	$\frac{-1}{2 \cdot \pi \cdot f \cdot Z'' \cdot A}$
where, A is an active area of two electrodes (cm^2).	i is the current (A), s is a scan rate (V s^{-1}), and V is the voltage window (V).	I is the discharge current (A), dV/dt is calculated from the discharge curve (excluding IR drop).	f is frequency (Hz), Z' is the imaginary impedance component (Ω).

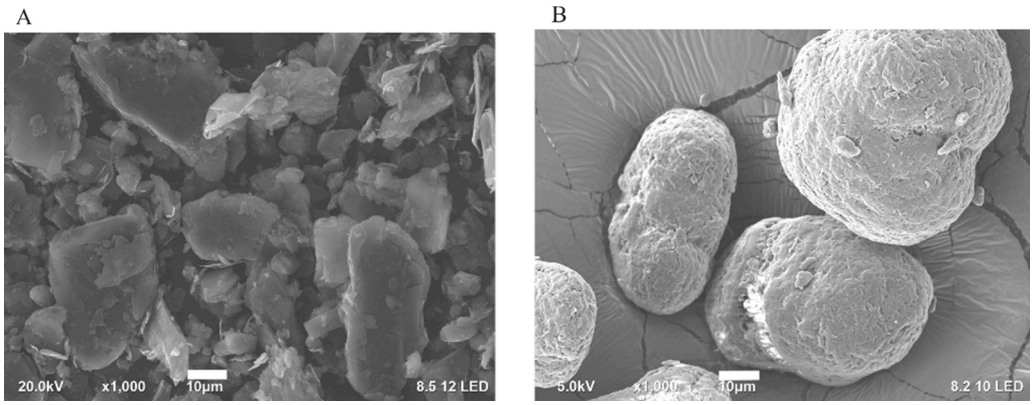

Fig. 1. SEM images of (A) graphite flakes and (B) nylon particles.

Considering the elemental composition of graphite (C – 99.99 At%, Si – 0.01 At%) and nylon (C – 92.24 At%, O – 6.23 At%, N – 1.21 At%, P – 0.12 At%, Ti – 0.10 At%, Si – 0.07 At%, Al – 0.02 At%, Cu – 0.01 At%), a stick-like object inside the nylon agglomerate was identified as an encapsulated graphite flake with the length of about 12 μm. The corresponding EDX mapping of bare graphite and nylon are illustrated in Fig. S4 and S5, respectively.

Further, under the strongest magnification, various pores with an average diameter of 50 nm, demonstrated in Fig. 4(A and B), were observed on the surface of nylon particles throughout the whole width of the AM composite. The porosity formation among the polymer matrix is attributed to the excessive laser energy resulting in extremely high temperatures and therefore leading to polymer pyrolysis. Furthermore, the presence of carbonous additive intensifies the localized heating and facilitates pore formation [20].

The SEM images of the AM graphite/nylon electrode reveal the macroporous structure of the L-PDF-produced material. Graphite flakes, deposited at the surface of the nylon agglomerates, represent the formation of the percolating network along the AM graphite/nylon electrode, resulting in electrical conductivity [18,20,21]. Some of the graphite flakes were encapsulated within the polymer matrix. Isolation of the separated conducted particles is considered a dead material in the electrode composition. Whereas the prolongation of the conductive network among the polymer matrix with further exposition to the surface might facilitate the electrical conductivity of the AM electrode [16].

The surface area is one of the key parameters affecting the electrochemical performance. Therefore, the specific surface area of the AM composite was measured. A decline of the specific surface area was noted for the AM graphite/nylon electrode in comparison with bare graphite and nylon powders. Thus, the BET specific surface areas of graphite and nylon were calculated to be 7.2 $m^2\ g^{-1}$ and 1.5 $m^2\ g^{-1}$, respectively. While the BET specific surface area of the AM graphite/nylon composite was only 0.9 $m^2\ g^{-1}$, provoked by the L-PBF process causing the melting of nylon particles and subsequently resulting in the clogging of the available pores of the bare input powders [25].

The crystal structure of the compounds of the AM specimen has been determined via the XRD pattern (Fig. 5(A)). Graphite is characterized by a sharp peak at ~27° (*d*-spacing of 3.3 Å) corresponding to the (002) plane. Other peaks related to graphite were noted at ~45° (*d*-spacing of 2.01 Å), ~55° (*d*-spacing of 1.67 Å), and ~78° (*d*-spacing of 1.22 Å) associated, respectively, with the (101), (004), and (110) planes [26]. The XRD pattern of the original nylon powder shows two peaks at 21.2° and 22.4°, which are related to the γ-crystal form (100) and the α-crystal form (010/110), respectively [27]. All the peaks, related to graphite, have been observed on the diffractogram of the AM graphite/nylon electrode, confirming a high degree of graphitization of the carbonaceous material. While material transformations, caused by the L-PBF, resulted in the nylon crystallization exclusively in the γ-form, as observed in the AM composite diffractogram via the appearance of only one nylon peak at 21.2° (*d*-spacing of 4.18 Å).

The crystallographic structures of the AM graphite/nylon specimen and the input materials have been examined via Raman spectra (Fig. 5 (B)). Graphite in the composition of AM specimen has been represented by peaks at 1350 cm^{-1}, 1580 cm^{-1}, 2700 cm^{-1}, and 3250 cm^{-1} corresponding to D and G bands and their overtones D* and G*, respectively [28]. The D band, resulting from the breathing modes of disordered graphitic rings, indicates the disordered crystalline structure of graphite. While the G band, induced by the in-plane bond-stretching motion of pairs of sp^2 carbon atoms, is associated with the graphitization degree [29]. The relative intensity (I_D/I_G) between the D and G bands is used to estimate the number of defects in the material. The lower value of (I_D/I_G) corresponds to fewer defects. Therefore, the decrease in relative intensity from 0.48 for graphite to 0.18 for AM graphite/nylon composite reveals the positive effect of the temperature during AM process on the graphite structure [30]. Nylon has been indicated by the double peaks at 1063 – 1107 cm^{-1} and 2848 – 2883 cm^{-1}, related to C-C stretch and CH_2 symmetric stretching, respectively. Small peaks at 1296 cm^{-1} and 1437 cm^{-1} are respectively assigned to CH_2 twisting and CH_2 bending. NH stretching vibrations are represented by peaks at 1636 cm^{-1} and 3293 cm^{-1} [31].

Further, functional groups, observed in the FTIR spectra of the AM graphite/nylon specimen (Fig. 5(C)), belong to nylon. Particularly, a peak at 3299 cm^{-1} indicates the hydrogen-bonded N–H stretching vibrations (Amide A). A moderate peak at 3098 cm^{-1} relates to C–H stretching vibration bond (Amide B). Peaks at 2920 cm^{-1} and 2850 cm^{-1} are associated with asymmetric and symmetric C–H stretching vibrations, respectively. A band of peaks at 1635 cm^{-1}, 1561 cm^{-1}, and 1465 cm^{-1} correspond to the C=O stretching vibrations, C=N stretching vibration (Amid II band), and CH_2 symmetric deformation vibration, respectively [32,33]. A peak at 720 cm^{-1} indicates $\rho(CH_2)$ rocking [25]. The absence of recognizable peaks in the graphite spectra reveals its chemical inertness [34].

According to the conducted material characterization, the positions of the peaks in the XRD pattern and Raman spectra, and identified functionalities in FTIR spectra individually correspond to the input nylon (PA12) and graphite powders. Therefore, no chemical interaction between the components during L-PBF occurred. Nevertheless, some phase transformations of the input materials, caused by the heat during the L-PBF process, were noticed. Thus, the decrease in the number of defects in the graphite crystallographic structure was observed from the Raman spectra, and the transformation of nylon crystals exceptionally in the pseudo-hexagonal phase (γ- form) was defined by the XRD diffractogram.

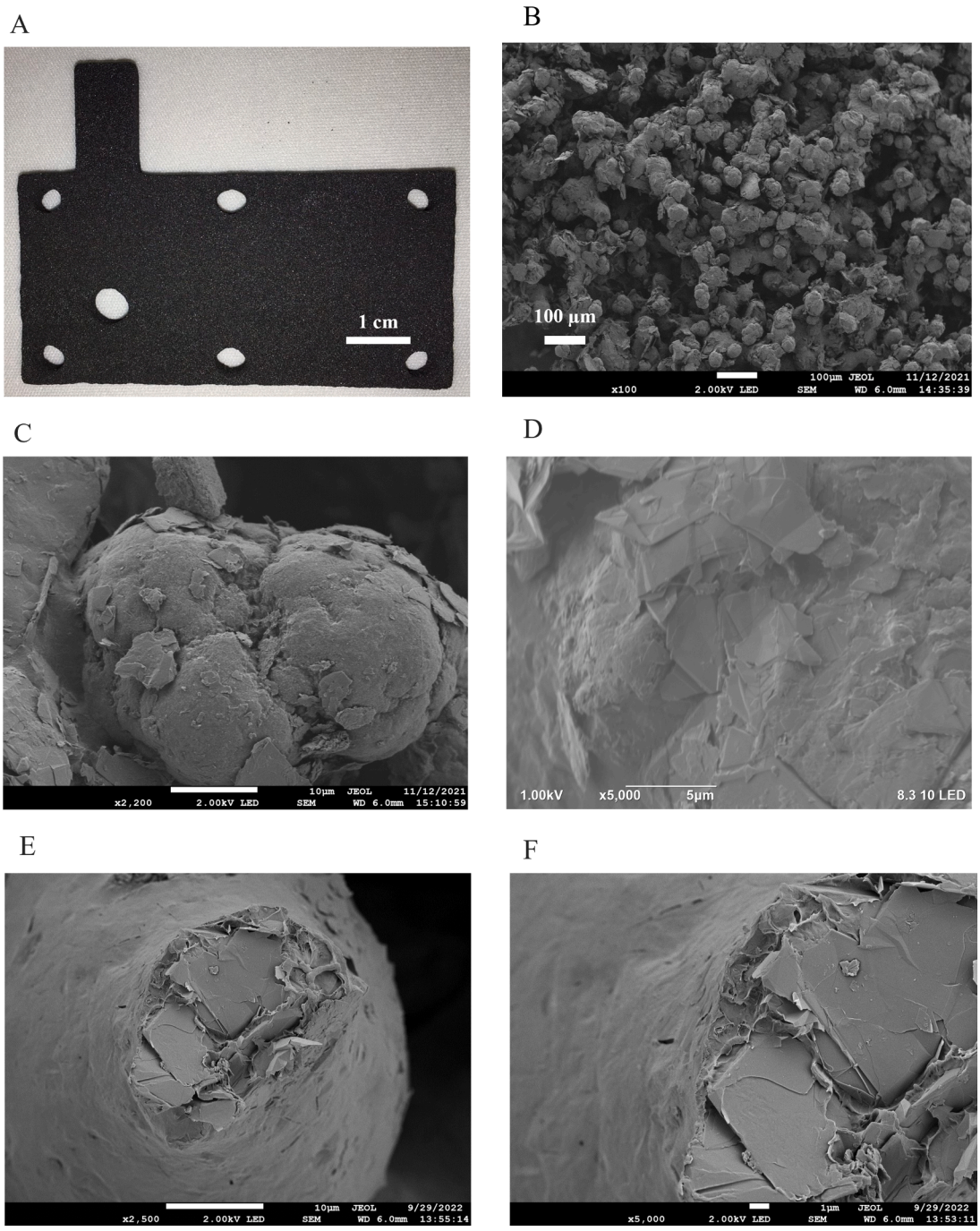

Fig. 2. (A) Digital image of the AM graphite/nylon electrode and (B) SEM image of its surface under 100 times magnification. SEM images of (C) fused nylon particles, covered by graphite flakes, and (D) graphite flakes irregularly distributed on the surface of nylon agglomerate. (E and F) Cryofractured cross-section area of the nylon agglomerate representing the encapsulated graphite flakes.

3.2. Electrochemical characterization

Two-electrode cell configuration, used for the electrochemical analyses, allows the simulation of real operating conditions of EES systems [2]. The electrochemical study on the AM graphite/nylon electrodes has been started from the CV to characterize the electrochemical reactions involved and identify sufficient applied electrical current used for GCD. Further, GCD cycling has been conducted to estimate the cyclability and retention capacity of the electrodes. EIS was carried out for the investigation of the resistive and diffusion characteristics of the materials [3].

The energy storage mechanism of the capacitive electrodes is based on the EDL formation at the electrode/electrolyte interface. Hence, no redox reactions may take place in the applied voltage window [35]. The determination of the usable voltage window depends on the decomposition of the electrolyte and irreversible reactions with the electrode. Therefore, the maximum voltage window for the aqueous electrolytes is 1 V [36]. Whereas the electrolyte nature determines the electrochemical performance of EES devices due to its ionic conductivity and charge compensation on the electrodes. To examine the behaviour of the AM graphite-nylon electrodes in electrolytes of different natures within various voltage windows, the CV has been carried out at 50 mV s^{-1} scan rate. The effect of the extended voltage windows in acidic, neutral, and alkaline electrolytes, respectively, is demonstrated in Fig. 6(A, D, G). The inflections observed with the increasing voltage range indicate the

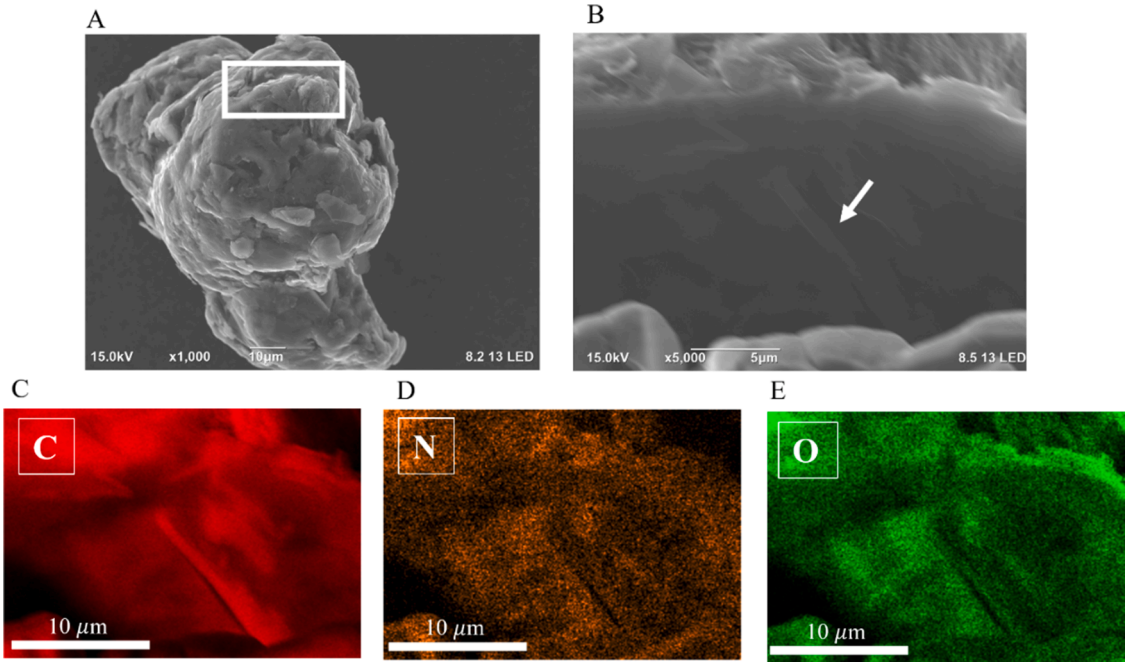

Fig. 3. (A) SEM image of a fused particle of the AM graphite/nylon electrode (white frame on the image corresponds to the area of cross-section). (B) A cross-section area onto the fused particle prepared by FIB. (C– E) EDX mapping of C, N, and O onto the cross-section area.

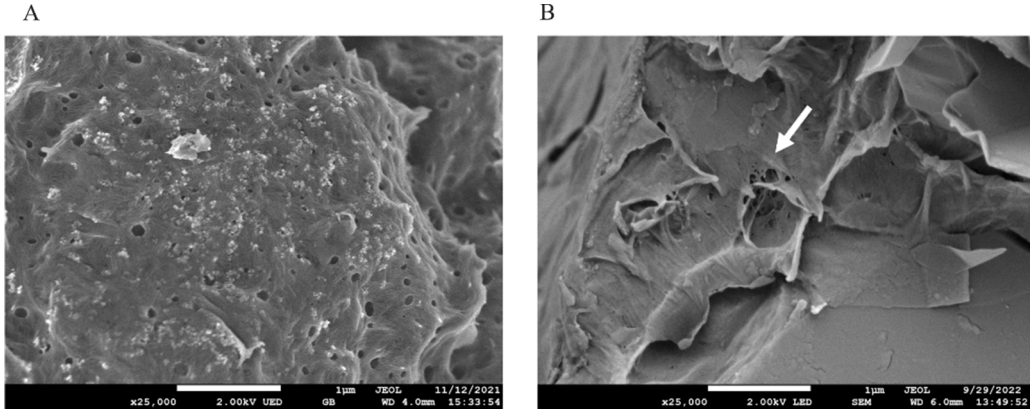

Fig. 4. SEM images of pores resulted from nylon pyrolysis during the L-PBF process. (A) The analyzed sample has been taken from (A) the surface and from the cryofractured cross-section area of the AM electrode.

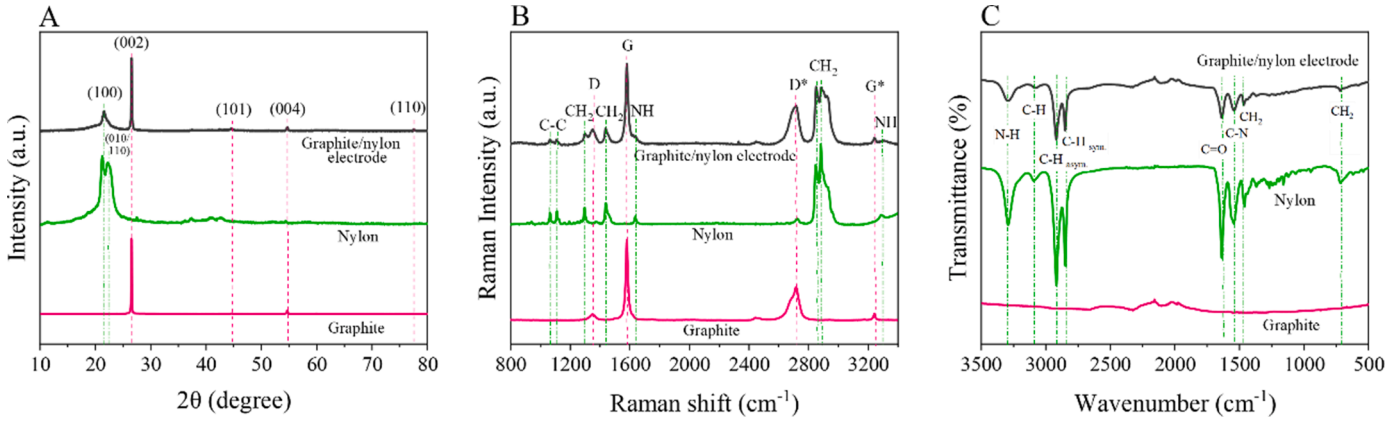

Fig. 5. (A) XRD pattern, (B) Raman spectra, and (C) FTIR spectra of the AM graphite/nylon electrode and input materials.

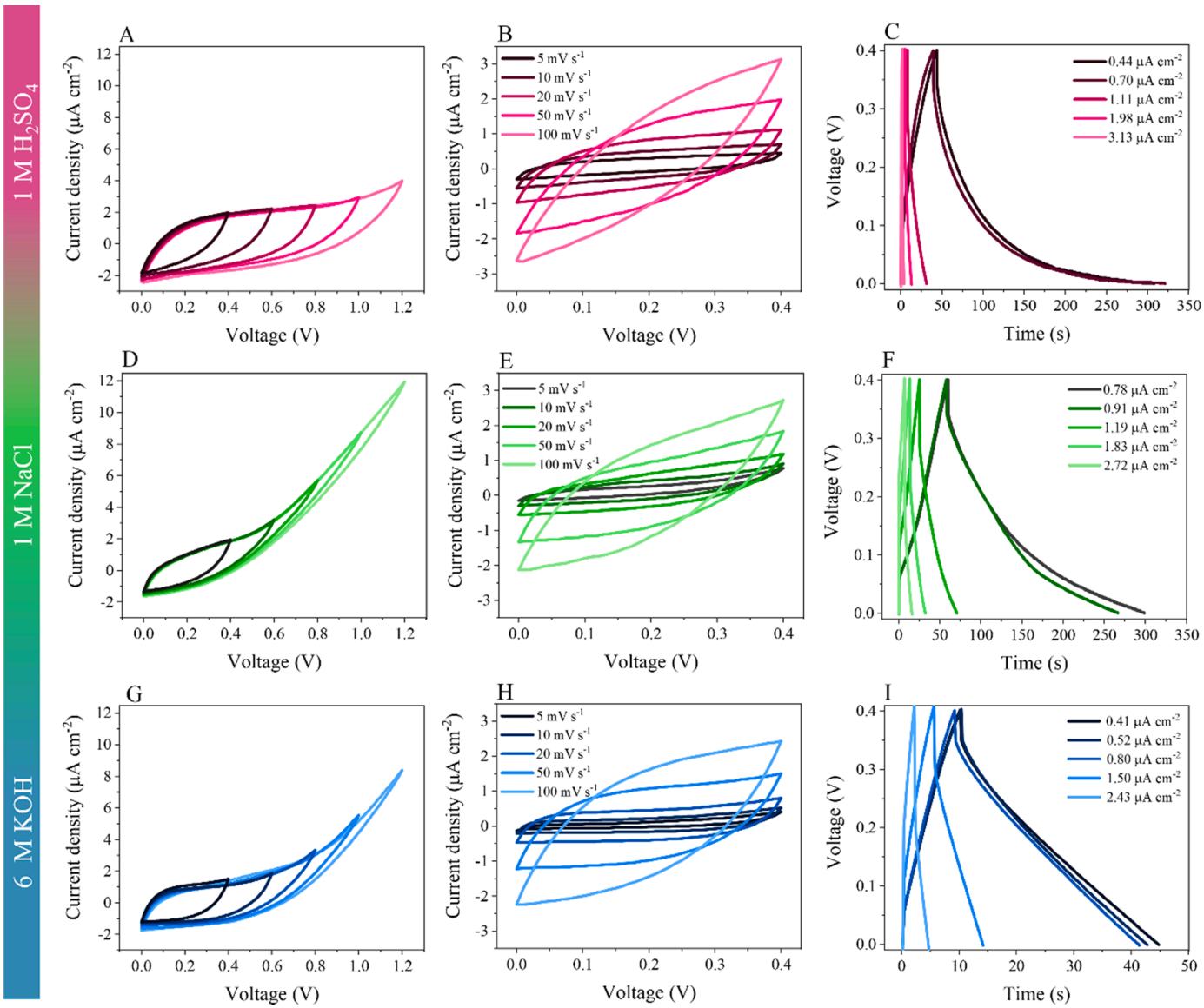

Fig. 6. Electrochemical characterization of the AM graphite/nylon electrodes in a two-electrode cell using three different electrolytes. (A, D, G) Extending voltage windows (at 50 mV s^{-1} scan rate). (B, E, H) CV curves at different scan rates. (C, F, I) GCD curves at different current densities.

decomposition of the electrolytes [2], resulting in redox reactions, and thus, deviation from the capacitive behaviour. Moreover, the gas evolution at a higher voltage may cause a rupture of the cell, provoking safety issues and performance degradation [36]. The early inflection has been already noticed at 0.6 V at the CV curve attributed to 1 M NaCl. While, no inflections have been observed before 0.8 V and 1.2 V, respectively, for 6 M KOH and 1 M H_2SO_4. Typically, a neutral electrolyte has a wider voltage window compared to acid and alkaline electrolytes, because of the lower activity of H^+ and OH^-. However, the earliest inflection occurred at the CV curve of 1 M NaCl, which might be related to the evolution of Cl^- [37], resulting in the narrowing of the electrochemical window. To avoid the effects of redox reactions accompanying the decomposition of the electrolytes and consider only the capacitive properties of the AM graphite-nylon electrodes, the voltage window of 0.4 V has been adjusted.

The CV curves recorded for the AM graphite/nylon electrodes in the different electrolytes at various scan rates are shown in Fig. 6(B, E, H). The obtained CV curves exhibit a quasi-rectangular shape, deviating from the ideal rectangular pattern. This might be related to the slowness of ion diffusion and/or the increase of the resistance, associated with the scan rate increase [38]. The values of anodic current, determined at a voltage of 0.4 V, are linearly proportional to the scan rates, as depicted in Fig. S6, confirming the electrostatic EDL charging on the electrodes [3,39]. The absence of the redox peaks suggests the reversible and kinetically facile charge-discharge process [40] and reveals the electrochemical inactivity of nylon in the electrode composition.

The GCD profiles of the AM graphite/electrodes, shown in Fig. 6(C, F, I), are quasi-triangular, indicating the deviation from the ideal capacitive behaviour and facing disruption with the EDL formation [41]. Sudden voltage drops (IR) observed at the discharge curves are directly associated with the internal resistance of the tested system, caused by a high ratio of insulating polymer in the AM electrode composition.

The effect of the electrolyte on the electrochemical performance of the AM graphite/nylon electrodes can be evaluated through the CV, GCD, and Nyquist plots, summarized in Fig. 7(A, B, C), respectively. Based on the recorded electrochemical data, the corresponding specific capacitances were calculated and presented in Fig. 7(D, E, F).

From Fig. 7(A), it is seen that the biggest area is covered by the CV curves, recorded at 20 mV s^{-1} scan rate in the acidic environment. While the CV curves obtained in neutral and alkaline electrolytes have smaller

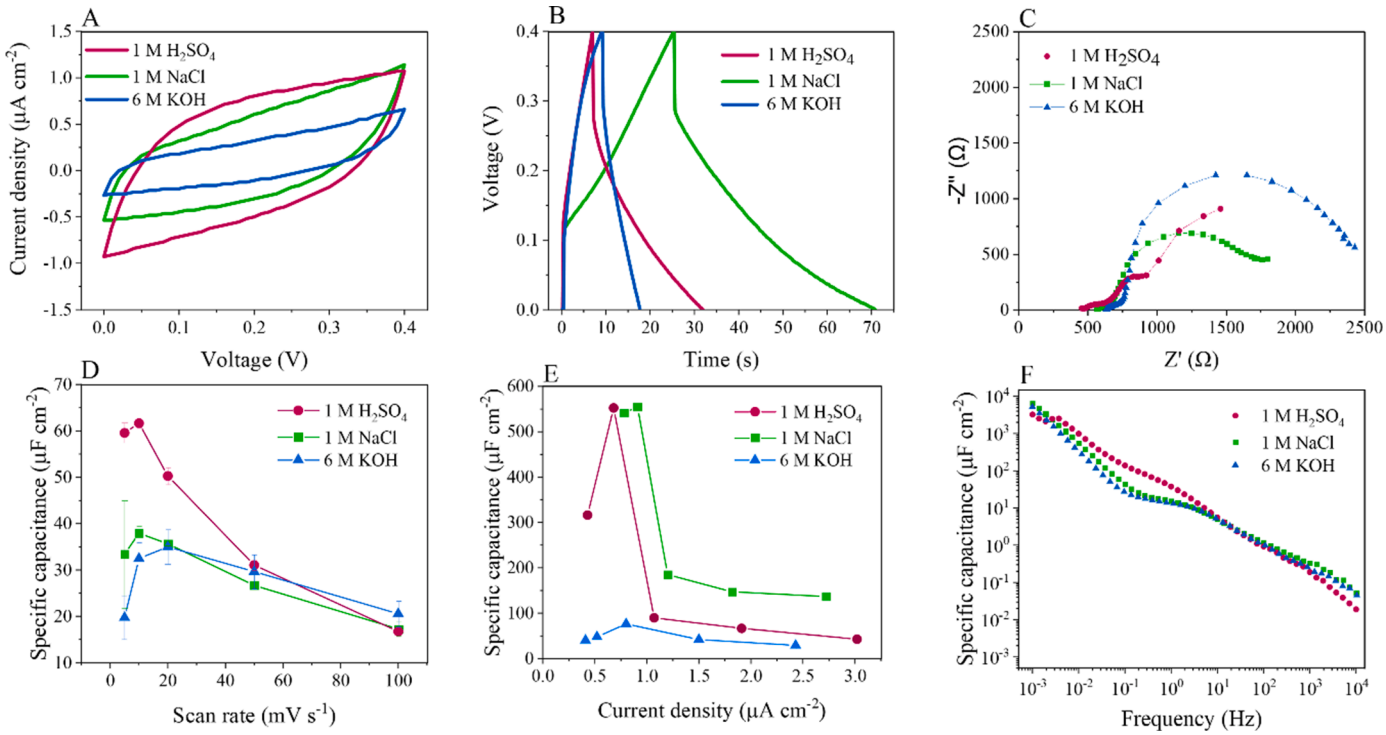

Fig. 7. (A) CV curves at 20 mV s^{-1} scan rate, (B) GCD curves at 1.19 μA cm^{-2}, (C) Nyquist plots of the AM graphite/nylon electrodes recorded in different electrolytes. Variation of the specific capacitances depending on (D) scan rates, (E) current densities, (F) frequencies.

performance areas, affecting the smaller values of the specific capacitance as depicted in Fig. 7(D). The higher specific capacitance observed in 1 M H_2SO_4 is in a good correlation with the high ionic conductivity of H^+ and HSO_4^- and their hydrated ion sizes (the parameters of the ions are listed in Table S3), which affect the higher current response during the CV [42]. While relatively comparable areas of the CV curves and similar values of the specific capacitance assigned to 1 M NaCl and 6 M KOH electrolytes indicate the unfavourable EDL formation in the alkaline electrolyte, even at its high ionic conductivity. From the GCD curve in Fig. 7(B) the longest discharged time was observed via using the neutral solution, resulting in a higher specific capacitance [43], as correspondingly depicted in Fig. 7(E).

Both Fig. 7(D) and Fig. 7(E) demonstrate unusual behaviour of the specific capacitance as a function of the scan rate and the current density, respectively. Generally, the specific capacitance decreases with the increase of the applied parameters because of the limited time, required for ions to diffuse into the interface of the electrode. However, the first points of the specific capacitance, calculated at 5 mV s^{-1} scan rate and the lowest value of current density, stand out from the general trend. Such an abnormality might be associated with the structural collapsing of carbon material under slow kinetic processes, causing reduced access to the electrode surface and therefore lower capacitance [39]. Nevertheless, the values of the specific capacitance decrease from the 61.7 μF cm^{-2} to 16.7 μF cm^{-2} in the acidic electrolyte, and from the 37.9 μF cm^{-2} to 17.2 μF cm^{-2} in the neutral electrolyte, while the scan rate increases from 10 mV s^{-1} to 100 mV s^{-1}. In the alkaline electrolyte, the highest value of the specific capacitance of 35 μF cm^{-2} is detected at 20 mV s^{-1} scan rate, and the lowest one of 20.5 μF cm^{-2} was noted at 100 mV s^{-1}. Analogously, the specific capacitance decreases from 552.5 μF cm^{-2} to 42.7 μF cm^{-2} in 1 M H_2SO_4, from 554.6 μF cm^{-2} to 136.9 μF cm^{-2} in 1 M NaCl, and from 76.43 μF cm^{-2} to 29 μF cm^{-2} in 6 M KOH, while the applied current densities increase.

Data obtained from EIS measurements were interpreted through Nyquist plots (Fig. 7(C)) and corresponding to Bode diagrams (Fig. S7(A, B, C)). Nyquist plot exhibits the imaginary part of the impedance as a function of the real impedance component recorded in the frequency range from 1 MHz to 1 mHz. The Bode diagram illustrates the measured phase angle and overall complex capacity towards frequency. Because of the inductive effects [35], which appeared at the higher frequencies, the experimental points above 10 kHz were removed from the plots. The Nyquist plots consist of small, compressed semicircles, that appeared at high frequencies, and large semicircles towards intermediate and low frequencies. The observed semicircles are typically assigned to the charge-transfer processes between the electrodes and the electrolytes, which are faster than diffusion processes. It means that the applied frequencies and the electrical conductivity of the electrolyte and the electrodes are insufficient to make a mass transfer available. Additionally, the absence of a vertical increase in the imaginary part of impedance for the plots of neutral and alkaline electrolytes implies that EDL formation has not been achieved [44]. While a non-linear component of the plot, recorded in the acidic electrolyte, indicates diffusion processes, which are feasible due to the ionic activity of 1 M H_2SO_4. Being in line with Nyquist plots, Bode diagrams confirm a resistive behaviour of the AM electrodes with a poor EDL formation [45].

A substantial contribution of the electrolyte to the impedance of the electrochemical cell has been already noted above. Furthermore, electrolyte resistance is the controlling factor of the cell impedance characteristics at higher frequencies. The intercepts at Z' axis provide an idea of the electrolyte resistance [46]. It is seen that the acidic electrolyte has a lower resistance, which is in correspondence with its higher conductivity. The internal resistances of the tested cell as a function of frequency are displayed in Fig. S8. Particularly, the internal resistances of the cell, evaluated at 1 kHz, are 476 Ω for the test with 1 M H_2SO_4, 571 Ω for 1 M NaCl, and 638 Ω for 6 M KOH. Considering that the resistance of graphite was about 7 Ω [47], a major contribution of the polymer matrix to the impedance can be defined. Nevertheless, the internal resistance of the graphite/nylon electrodes, printed by L-PBF, is rather low compared to 8300 Ω for the electrodes, produced by material extrusion [48]. The changes in the capacitance depending on frequencies are presented in Fig. 7(F). All the curves demonstrate a typical capacitance decline within the frequency increase. Since ions do not have sufficient time to diffuse into the pores of the electrode surface under the high frequency.

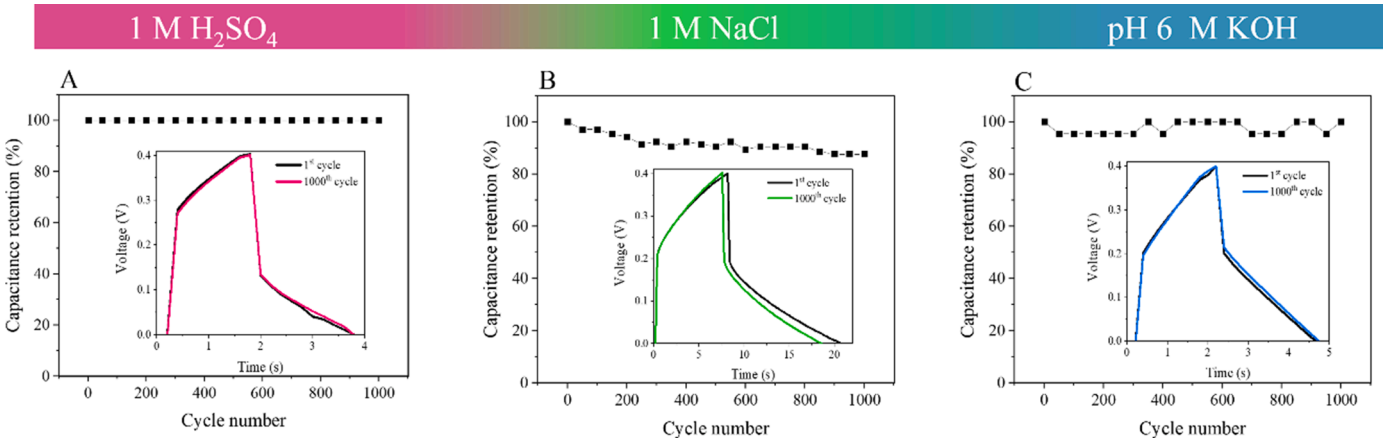

Fig. 8. Cyclic stability of two-electrode cell with the AM graphite/nylon electrodes operating in (A) 1 M H_2SO_4 at 3.13 μA cm^{-2}, (B) 1 M NaCl at 2.72 μA cm^{-2}, (C) 6 M KOH at 2.43 μA cm^{-2} for 1000 cycles. Insets are the 1st and the 1000th charging-discharging cycles.

Cyclic stability is a significant parameter considered for the practical application of SCs. The AM graphite/nylon electrodes have been tested at current densities of 3.13 μA cm^{-2}, 2.72 μA cm^{-2}, and 2.43 μA cm^{-2} in 1 M H_2SO_4, 1 M NaCl, and 6 M KOH, respectively, during 1000 cycles (Fig. 8).

The electrodes demonstrate excellent capacitive retention using 1 M H_2SO_4 (Fig. 8(A)). The decay of the available capacity of up to 12% has been calculated for the electrodes tested in 1 M NaCl (Fig. 8(B)). Some intermittent fluctuations of 5% in the capacitive retention have been noticed within the operating in 6 M KOH (Fig. 8(C)). The insets in Fig. 8 illustrate similar GCD curves after the 1st and 1000th charging-discharging cycles indicating the stability of the long-term operation of the EES device equipped with the AM graphite/nylon electrodes.

Based on the obtained results, 1 M H_2SO_4 might be considered a preferable electrolyte for the AM graphite/nylon electrodes because of the promoting high values of the specific capacitance, low resistance, and outstanding cyclic stability. The neutral electrolyte might also be recommended for these electrodes, if NaCl will be substituted with an alternative electrolyte to avoid chlorine evolution, resulting in the narrowing of the operating voltage window. The lower electrochemical parameters observed by using the alkaline electrolyte might be defined by unfavorable affiliation between OH- ions and the electrode composition. The conducted EIS analyses revealed high resistance of the AM graphite/nylon electrodes and poor EDL formation, resulting in quite low values of the specific capacitance. These observations might be explained by using a non-conductive printing matrix and by the electrode geometry. It is known that the electrochemical performance strongly depends on the electrode dimensions. Fig. S9 demonstrates the electrochemical performance of the AM graphite/nylon electrodes of smaller sizes. The key advantage of the electrode size reduction is the decrease of the internal cell resistance that contributes to the increase of the electrochemical parameters. Therefore, further investigation into the effect of the electrode geometry is needed. Despite the listed limitations, the electrochemical capability of the freestanding electrodes printed by L-PBF was presented.

Porous and customizable carbon-based electrodes can be produced by the L-PBF process. Their efficiency for electrochemical performance requires significant improvements and rearrangements. Despite, the high weight ratio of the conductive additive in the printing mixture, causing the formation of the conductive network at the surface and inside nylon agglomerates, the electrical conductivity of the whole AM graphite/nylon electrode (ca. 1×10^{-2} S cm^{-1}) is very low in comparison with the reference value of graphite pellets (ca. 63×10^{-2} S cm^{-1}) [18]. The losses of the electrical conductivity of the L-PBF-printed electrodes attribute not only to the insulating behaviour of the nylon but also to the porous structure of the object. It is known that the electrical conductivity rises as the porosity of the object declines [49]. Thus, there is a choice between electrical conductivity and porosity here. To go around this obstacle, the replacement of the graphite flakes with carbon plates of a bigger size or carbon fibers might be proposed. The prolate form of conductive additives will form a continuous conductive network in line with the percolation theory [20].

Other practical recommendations might be considered:

i) increasing the conductivity of the additive manufacturing material by the post-treatment focusing on the degradation of the polymer matrix by applying chemical reagents. As recently reported, the encapsulated active additives were exposed from the bulk to the surface due to the partial dissolving of the polymer [50,51] resulting in the enhancement of the electrochemical properties of the AM electrodes, while keeping the mechanical properties unaltered [52]. In addition, the increased conductivity of AM electrodes along with the preservation of the 3D structure can be achieved via thermal annealing [53];
ii) increasing the surface hydrophilicity to improve the accessibility of the surface to the electrolyte;
iii) adjusting the AM electrode surface with the suitable porous structure to provide the passage of the electrolyte through macro- and mesoporous and ions accumulation in micropores;
iv) functionalizing the surface of AM electrodes with the desired species.

4. Conclusion

Fabrication of the material ensuring its printability and meeting the consumer requirements is the next step in the development and promotion of AM technologies for different applications and industrial production of the systems. In this research, the electrochemical properties of the freestanding AM graphite/nylon electrodes have been studied in order to confirm the concept of the freestanding AM electrodes utilized for EES devices. The electrodes reveal their applicability for electrochemical applications demonstrating the capacitive behaviour in acidic, neutral, and alkaline electrolytes. The outstanding cyclic stability of the AM graphite/nylon electrodes with an average 95% retention of specific capacitance was observed during the experiments. The advantages of the choice of the L-PBF for electrodes were confirmed by the material characterization study that represented the retention of the individual properties of the electrode components, providing the conductive network among graphite particles. Despite, the electrochemical characterization revealing that nylon is an inert component of the AM electrode and does not provoke redox reactions, a dramatic effect on the electrode resistance has been observed because of the

insulating nature of the polymer. The present study is a promising step toward the implementation of AM technologies in the production of electrochemically active materials. Further research on the increase of the carbonous ratio in the electrode composition, the printing of the precise structure, and post-printing treatment will facilitate the usability of the AM electrodes.

CRediT authorship contribution statement

O.P.: conceptualization, methodology, material characterization, and electrochemical study, writing - original draft. **L.K.**: modelling and additive manufacturing of the electrodes. **E.L.**: methodology, material characterization, supervising of the experimental work, writing - review & editing. **M.H.**: supervision of additive manufacturing, writing - review & editing. **H.P.**: writing - review & editing. **E.R.**: conceptualization, supervision & support, writing - review & editing, resources, project administration.

Declaration of Competing Interest

The authors declare that they have no known competing financial interests or personal relationships that could have appeared to influence the work reported in this paper.

Data Availability

Data will be made available on request.

Acknowledgments

The authors acknowledge European Regional Development Fund, REACT-EU, South-Savo Regional Council (Project no. A78710), Academy of Finland (Grant no. 330076 and 325002) and Maa- ja vesitekniikan tuki ry (Grant no. 13-8210-7). The research was also supported by the encouragement grant from Finnish Foundation for Technology Promotion (Grant no. 8168). The authors are grateful to Dr. Liisa Puro and Dr. Timo Laakso for carrying out XRD, FTIR, SEM, and Raman analyses.

Supplementary materials

Supplementary material associated with this article can be found, in the online version, at doi:10.1016/j.electacta.2022.141732.

References

[1] S.B. Tsai, Y. Xue, J. Zhang, Q. Chen, Y. Liu, J. Zhou, W. Dong, Models for forecasting growth trends in renewable energy, Renew. Sustain. Energy Rev. (2017), https://doi.org/10.1016/j.rser.2016.06.001.
[2] J. Castro-Gutiérrez, A. Celzard, V. Fierro, Energy storage in supercapacitors: focus on tannin-derived carbon electrodes, Front. Mater. 7 (2020) 1–25, https://doi.org/10.3389/fmats.2020.00217.
[3] S. Zhang, N. Pan, Supercapacitors performance evaluation, Adv. Energy Mater. 5 (2015) 1–19, https://doi.org/10.1002/aenm.201401401.
[4] D.K. Kampouris, X. Ji, E.P. Randviir, C.E. Banks, A new approach for the improved interpretation of capacitance measurements for materials utilised in energy storage, RSC Adv 5 (2015) 12782–12791, https://doi.org/10.1039/c4ra17132b.
[5] T. Chu, S. Park, K. Fu, 3D printing-enabled advanced electrode architecture design, Carbon Energy 3 (2021) 424–439, https://doi.org/10.1002/cey2.114.
[6] J. Li, F. Ye, S. Vaziri, M. Muhammed, M.C. Lemme, M. Östling, Efficient inkjet printing of graphene, Adv. Mater. 25 (2013) 3985–3992, https://doi.org/10.1002/adma.201300361.
[7] L.M. Samyn, R.S. Babu, M. Devendiran, A.L.F. de Barros, Electropolymerization of p-phenylenediamine films on carbon fiber fabrics electrode for flexible supercapacitors: surface and electrochemical characterizations, Ionics (Kiel) 26 (2020) 3041–3050, https://doi.org/10.1007/s11581-020-03562-0.
[8] A. Ambrosi, M. Pumera, 3D-printing technologies for electrochemical applications, Chem. Soc. Rev. 45 (2016) 2740–2755, https://doi.org/10.1039/c5cs00714c.
[9] N.V. Blaž, L.D. Živanov, M.G. Kisić, A.B. Menićanin, Fully 3D printed rolled capacitor based on conductive ABS composite electrodes, Electrochem. Commun. 134 (2022) 3–7, https://doi.org/10.1016/j.elecom.2021.107178.
[10] T. Reinheimer, V. Baumann, J.R. Binder, Fabrication of flexible multilayer composite capacitors using inkjet printing, Nanomaterials (2020), https://doi.org/10.3390/nano10112302.
[11] P.F. Flowers, C. Reyes, S. Ye, M.J. Kim, B.J. Wiley, 3D printing electronic components and circuits with conductive thermoplastic filament, Addit. Manuf. (2017), https://doi.org/10.1016/j.addma.2017.10.002.
[12] Senvol database of industrial AM machines and materials, (2022) 154. http://senvol.com/5_material-results/(accessed October 18, 2022).
[13] P. Blyweert, V. Nicolas, V. Fierro, A. Celzard, 3D printing of carbon-based materials: a review, Carbon N. Y. 183 (2021) 449–485, https://doi.org/10.1016/j.carbon.2021.07.036.
[14] C. Zhu, T. Liu, F. Qian, T.Y.J. Han, E.B. Duoss, J.D. Kuntz, C.M. Spadaccini, M. A. Worsley, Y. Li, Supercapacitors based on three-dimensional hierarchical graphene aerogels with periodic Macropores, Nano Lett 16 (2016) 3448–3456, https://doi.org/10.1021/acs.nanolett.5b04965.
[15] P. Chang, H. Mei, S. Zhou, K.G. Dassios, L. Cheng, 3D printed electrochemical energy storage devices, J. Mater. Chem. A. 7 (2019) 4230–4258, https://doi.org/10.1039/c8ta11860d.
[16] A. Maurel, M. Haukka, E. MacDonald, L. Kivijärvi, E. Lahtinen, H. Kim, M. Armand, A. Cayla, A. Jamali, S. Grugeon, L. Dupont, S. Panier, Considering lithium-ion battery 3D-printing via thermoplastic material extrusion and polymer powder bed fusion, Addit. Manuf. (2021), https://doi.org/10.1016/j.addma.2020.101651.
[17] M. Korpela, N. Riikonen, H. Piili, Technical, economic and societal effects of manufacturing 4.0, Tech. Econ. Soc. Eff. Manuf. 4.0. (2020) 17–41, https://doi.org/10.1007/978-3-030-46103-4.
[18] E. Lahtinen, E. Kukkonen, J. Jokivartio, J. Parkkonen, J. Virkajärvi, L. Kivijärvi, M. Ahlskog, M. Haukka, Preparation of highly porous carbonous electrodes by selective laser sintering, ACS Appl. Energy Mater. 2 (2019) 1314–1318, https://doi.org/10.1021/acsaem.8b01881.
[19] C.Y. Lee, S. Sayyar, P.J. Molino, G.G. Wallace, A robust 3D printed multilayer conductive graphene/polycaprolactone composite electrode, Mater. Chem. Front. 4 (2020) 1664–1670, https://doi.org/10.1039/c9qm00780f.
[20] K.K. Athreya Siddharth Ram, D. Suman, Processing and characterization of a carbon black-filled electrically conductive Nylon-12 nanocomposite produced by selective laser sintering, Mater. Sci. Eng. A. 527 (2010) 2637–2642, https://doi.org/10.1016/j.msea.2009.12.028.
[21] R. Hong, Z. Zhao, J. Leng, J. Wu, J. Zhang, Two-step approach based on selective laser sintering for high performance carbon black/polyamide 12 composite with 3D segregated conductive network, Compos. Part B Eng. 176 (2019), 107214, https://doi.org/10.1016/j.compositesb.2019.107214.
[22] A.H. Espera, A.D. Valino, J.O. Palaganas, L. Souza, Q. Chen, R.C. Advincula, 3D printing of a robust Polyamide-12-Carbon black composite via selective laser sintering: thermal and electrical conductivity, Macromol. Mater. Eng. 304 (2019) 1–8, https://doi.org/10.1002/mame.201800718.
[23] F. Lupone, E. Padovano, O. Ostrovskaya, A. Russo, C. Badini, Innovative approach to the development of conductive hybrid composites for selective laser sintering, Compos. Part A Appl. Sci. Manuf. 147 (2021), 106429, https://doi.org/10.1016/j.compositesa.2021.106429.
[24] K. Kalaitzidou, H. Fukushima, L.T. Drzal, A route for polymer nanocomposites with engineered electrical conductivity and percolation threshold, Materials (Basel) (2010), https://doi.org/10.3390/ma3021089.
[25] G.S. Martynková, A. Slíva, G. Kratošová, K.Č. Barabaszová, S. Študentová, J. Klusák, S. Brožová, T. Dokoupil, S. Holešová, Polyamide 12 materials study of morpho-structural changes during laser sintering of 3d printing, Polymers (Basel) 13 (2021), https://doi.org/10.3390/polym13050810.
[26] Z.Q. Li, C.J. Lu, Z.P. Xia, Y. Zhou, Z. Luo, X-ray diffraction patterns of graphite and turbostratic carbon, Carbon N. Y. 45 (2007) 1686–1695, https://doi.org/10.1016/j.carbon.2007.03.038.
[27] B. Van Hooreweder, D. Moens, R. Boonen, J.P. Kruth, P. Sas, On the difference in material structure and fatigue properties of nylon specimens produced by injection molding and selective laser sintering, Polym. Test. 32 (2013) 972–981, https://doi.org/10.1016/j.polymertesting.2013.04.014.
[28] S. Reich, C. Thomsen, Raman spectroscopy of graphite, Philos. Trans. R. Soc. A Math. Phys. Eng. Sci. 362 (2004) 2271–2288, https://doi.org/10.1098/rsta.2004.1454.
[29] A. Ferrari, J. Robertson, Interpretation of Raman spectra of disordered and amorphous carbon, Phys. Rev. B - Condens. Matter Mater. Phys. 61 (2000) 14095–14107, https://doi.org/10.1103/PhysRevB.61.14095.
[30] S. Naghdi, K.Y. Rhee, M.T. Kim, B. Jaleh, S.J. Park, Atmospheric chemical vapor deposition of graphene on molybdenum foil at different growth temperatures, Carbon Lett 18 (2016) 37–42, https://doi.org/10.5714/CL.2016.18.037.
[31] P.J. Hendra, W.F. Maddams, I.A.M. Royaud, H.A. Willis, V. Zichy, The application of Fourier transform Raman spectroscopy to the identification and characterization of polyamides-I. Single number nylons, Spectrochim. Acta Part A Mol. Spectrosc. 46 (1990) 747–756, https://doi.org/10.1016/0584-8539(90)80031-S.
[32] N. Ma, W. Liu, L. Ma, S. He, H. Liu, Z. Zhang, A. Sun, M. Huang, C. Zhu, Crystal transition and thermal behavior of Nylon 12, E-Polymers 20 (2020) 346–352, https://doi.org/10.1515/epoly-2020-0039.
[33] B.M. De Campos, P.S. Calefi, K.J. Ciuffi, E.H. De Faria, L.A. Rocha, E.J. Nassar, J.V. L. Silva, M.F. Oliveira, I.A. Maia, Coating of polyamide 12 by sol-gel methodology, J. Therm. Anal. Calorim. 115 (2014) 1029–1035, https://doi.org/10.1007/s10973-013-3384-9.
[34] D. Galpaya, M. Wang, G. George, N. Motta, E. Waclawik, C. Yan, Preparation of graphene oxide/epoxy nanocomposites with significantly improved mechanical properties, J. Appl. Phys. (2014) 116, https://doi.org/10.1063/1.4892089.

[35] F. Lufrano, P. Staiti, M. Minutoli, Evaluation of nafion based double layer capacitors by electrochemical impedance spectroscopy, J. Power Sources. 124 (2003) 314–320, https://doi.org/10.1016/S0378-7753(03)00589-5.
[36] C. Zhong, Y. Deng, W. Hu, J. Qiao, L. Zhang, J. Zhang, A review of electrolyte materials and compositions for electrochemical supercapacitors, Chem. Soc. Rev. 44 (2015) 7484–7539, https://doi.org/10.1039/c5cs00303b.
[37] W. Wei, J. Xu, W. Chen, L. Mi, J. Zhang, A review of sodium chloride-based electrolytes and materials for electrochemical energy technology, J. Mater. Chem. A. 10 (2022) 2637–2671, https://doi.org/10.1039/d1ta09371a.
[38] N. Lima, A.C. Baptista, B.M.M. Faustino, S. Taborda, A. Marques, I. Ferreira, Carbon threads sweat-based supercapacitors for electronic textiles, Sci. Rep. 10 (2020) 1–10, https://doi.org/10.1038/s41598-020-64649-2.
[39] D. Sridhar, H. Yu, J.-L. Meunier, S. Omanovic, Carbon nano-fiber forest foundation for ruthenium oxide pseudo-electrochemical capacitors, Mater. Adv. 1 (2020) 215–227, https://doi.org/10.1039/d0ma00023j.
[40] C. Zhao, C. Wang, R. Gorkin, S. Beirne, K. Shu, G.G. Wallace, Three dimensional (3D) printed electrodes for interdigitated supercapacitors, Electrochem. Commun. 41 (2014) 20–23, https://doi.org/10.1016/j.elecom.2014.01.013.
[41] R. Gusmão, M.P. Browne, Z. Sofer, M. Pumera, The capacitance and electron transfer of 3D-printed graphene electrodes are dramatically influenced by the type of solvent used for pre-treatment, Electrochem. Commun. 102 (2019) 83–88, https://doi.org/10.1016/j.elecom.2019.04.004.
[42] A.A. Iurchenkova, E.V. Lobiak, A.A. Kobets, A.N. Kolodin, A. Stott, S.R.P. Silva, E. O. Fedorovskaya, A complex study of the dependence of the reduced graphite oxide electrochemical behavior on the annealing temperature and the type of electrolyte, Electrochim. Acta. 370 (2021), 137832, https://doi.org/10.1016/j.electacta.2021.137832.
[43] H. Wu, X. Wang, L. Jiang, C. Wu, Q. Zhao, X. Liu, B. Hu, L. Yi, The effects of electrolyte on the supercapacitive performance of activated calcium carbide-derived carbon, J. Power Sources. 226 (2013) 202–209, https://doi.org/10.1016/j.jpowsour.2012.11.014.
[44] E. Redondo, M. Pumera, MXene-functionalised 3D-printed electrodes for electrochemical capacitors, Electrochem. Commun. 124 (2021), 106920, https://doi.org/10.1016/j.elecom.2021.106920.
[45] N.O. Laschuk, E.B. Easton, O.V. Zenkina, Reducing the resistance for the use of electrochemical impedance spectroscopy analysis in materials chemistry, RSC Adv 11 (2021) 27925–27936, https://doi.org/10.1039/d1ra03785d.
[46] B.A. Mei, O. Munteshari, J. Lau, B. Dunn, L. Pilon, Physical interpretations of nyquist Plots for EDLC electrodes and devices, J. Phys. Chem. C. 122 (2018) 194–206, https://doi.org/10.1021/acs.jpcc.7b10582.
[47] X.H. Dai, H.X. Fan, J.J. Zhang, S.J. Yuan, Sewage sludge-derived porous hollow carbon nanospheres as high-performance anode material for lithium ion batteries, Electrochim. Acta. 319 (2019) 277–285, https://doi.org/10.1016/j.electacta.2019.07.006.
[48] J.U. S, S. Goel, Surface modified 3D printed carbon bioelectrodes for glucose/O2 enzymatic biofuel cell: Comparison and optimization, Sustain, Energy Technol. Assessments. 42 (2020), 100811, https://doi.org/10.1016/j.seta.2020.100811.
[49] J.M. Montes, F.G. Cuevas, J. Cintas, Porosity effect on the electrical conductivity of sintered powder compacts, Appl. Phys. A Mater. Sci. Process. 92 (2008) 375–380, https://doi.org/10.1007/s00339-008-4534-y.
[50] E. Redondo, J. Muñoz, M. Pumera, Green activation using reducing agents of carbon-based 3D printed electrodes: Turning good electrodes to great, Carbon N. Y. 175 (2021) 413–419, https://doi.org/10.1016/j.carbon.2021.01.107.
[51] D.M. Wirth, M.J. Sheaff, J.V. Waldman, M.P. Symcox, H.D. Whitehead, J.D. Sharp, J.R. Doerfler, A.A. Lamar, G. Leblanc, Electrolysis activation of fused-filament-fabrication 3D-printed electrodes for electrochemical and spectroelectrochemical analysis, Anal. Chem. 91 (2019) 5553–5557, https://doi.org/10.1021/acs.analchem.9b01331.
[52] M. Schneider, N. Fritzsche, A. Puciul-Malinowska, A. Baliś, A. Mostafa, I. Bald, S. Zapotoczny, A. Taubert, Surface etching of 3D printed poly(lactic acid) with NaOH: a systematic approach, Polymers (Basel) (2020), https://doi.org/10.3390/POLYM12081711.
[53] F. Novotný, V. Urbanová, J. Plutnar, M. Pumera, Preserving fine structure details and dramatically enhancing electron transfer rates in graphene 3D-Printed electrodes via thermal annealing: toward nitroaromatic explosives sensing, ACS Appl. Mater. Interfaces. (2019), https://doi.org/10.1021/acsami.9b06683.